

PAPER • OPEN ACCESS

Cobalt porphyrin/molybdenum disulfide nanoensembles for light-assisted electrocatalytic water oxidation and selective hydrogen peroxide production

To cite this article: Dimitrios K Perivoliotis *et al* 2023 *2D Mater.* **10** 014007

View the [article online](#) for updates and enhancements.

You may also like

- [Structural and Electrochemical Identification of CoFe Pnictide Catalysts Affecting the Performance of the Oxygen Evolution Reaction](#)
Ui Young Lee, Dong In Jeong, Hyung Wook Choi et al.
- [Carbon-Encapsulated Cobalt Phosphide Catalyst for Efficient Electrochemical Synthesis of Hydrogen Peroxide](#)
Xishuang Guo, Longhai Pan, Jiuyang Yu et al.
- [Green fabrication of ultrafine N-Mo_xC/CoP hybrids for boosting electrocatalytic water reduction](#)
Xiaomei Yu, Wei Shi, Jiajiao Wei et al.

OPEN ACCESS



PAPER

Cobalt porphyrin/molybdenum disulfide nanoensembles for light-assisted electrocatalytic water oxidation and selective hydrogen peroxide production

RECEIVED
26 May 2022REVISED
20 August 2022ACCEPTED FOR PUBLICATION
15 September 2022PUBLISHED
28 October 2022

Original content from this work may be used under the terms of the [Creative Commons Attribution 4.0 licence](#).

Any further distribution of this work must maintain attribution to the author(s) and the title of the work, journal citation and DOI.



Dimitrios K Perivoliotis^{1,2,†,*} , Christina Stangel^{1,†} , Yuta Sato³ , Kazu Suenaga⁴ and Nikos Tagmatarchis^{1,*}

¹ Theoretical and Physical Chemistry Institute, National Hellenic Research Foundation, 48 Vassileos Constantinou Avenue, 11635 Athens, Greece

² Department of Physics, Umeå University, 90187 Umeå, Sweden

³ Nanomaterials Research Institute, National Institute of Advanced Industrial Science and Technology (AIST), 1-1-1 Higashi, Tsukuba, Ibaraki 305-8565, Japan

⁴ The Institute of Scientific and Industrial Research (SANKEN), Osaka University, Mihogaoka 8-1, Ibaraki, Osaka 567-0047, Japan

† These authors contributed equally to this work.

* Authors to whom any correspondence should be addressed.

E-mail: dimperiv@eie.gr and tagmatar@eie.gr

Keywords: bifunctional photo/electrocatalysts, water oxidation, hydrogen peroxide, renewable fuels, transition metal dichalcogenides, cobalt porphyrins

Supplementary material for this article is available [online](#)

Abstract

The development of photo/electroactive catalysts sustainably producing hydrogen from water splitting and selectively hydrogen peroxide is of paramount importance to alleviate climate change effects. Herein, an anionic cobalt porphyrin (CoP) derivative is electrostatically interfaced with a positively charged modified molybdenum disulfide (MoS₂), forming CoP/MoS₂, which is accordingly employed as nonprecious photo/electrocatalyst for water oxidation reaction (WOR) and selective H₂O₂ production. According to the results, CoP/MoS₂ shows remarkable bifunctional photo/electrocatalytic performance for WOR and 2e⁻ pathway O₂ reduction reaction (ORR) in alkaline electrolyte. Upon visible light irradiation, electrochemical measurements on a fluorine-doped tin oxide (FTO) coated glass electrode reveal an onset potential of 0.595 mV (ORR) and 1.575 mV (WOR) vs. reversible hydrogen electrode, being improved by approximately 80 mV, in both cases, compared to the dark conditions. Notably, the use of the FTO set-up not only enabled us to evaluate the photo/electrocatalytic activity of the CoP/MoS₂ nanoensemble but also mimics the practical conditions in photo/electrochemical devices. The outstanding bifunctional photo/electrocatalytic performance of CoP/MoS₂ is attributed to (a) the use of CoP as versatile single-atom molecular catalyst and photosensitizer (b) the strong ion-pair interactions between cationic modified MoS₂ and the anionic CoP derivative, which prevent aggregation, ensuring better accessibility of the reactants to cobalt active sites, and (c) the co-existence of 1T and 2H phase at modified MoS₂, offering improved electrical conductivity and intrinsic electrocatalytic activity along with enhanced intraensemble electronic interactions upon illumination. This work is expected to inspire the design of advanced and low-cost materials for the sustainable production of renewable fuels.

1. Introduction

The sustainable production of renewable fuels is central to eliminate the carbon dioxide emission and therefore to mitigate the climate change effects.

Water-splitting by electrolysis is regarded as an eco-friendly way to produce renewable fuel in the form of hydrogen (H₂) [1]. Indeed, H₂ is a promising alternative to replace fossil fuels and can be produced in a water electrolyzer consisting of a water oxidation

reaction (WOR) anode and a hydrogen evolution reaction (HER) cathode. Notably, the anodic half-reaction, i.e. WOR, is the most challenging part of the overall water-splitting process [2]. Besides H₂, hydrogen peroxide (H₂O₂) has also attracted significant attention as energy carrier due to its high volumetric energy density and easy storage, while the two-electron electrochemical reduction of dioxygen is considered as a sustainable approach to generate H₂O₂ in view to replace the current anthraquinone process [3–5]. Given the sluggish kinetics of the involved electrochemical reactions, namely, water oxidation and oxygen reduction reaction (ORR) for H₂O₂ production, the core scientific challenge for the commercialization of such systems lies in the development of highly active and selective multifunctional electrocatalysts composed of earth-abundant and non-critical elements [6–9]. Presently, cutting-edge electrocatalysts for ORR are based on platinum, while for water oxidation are iridium and ruthenium oxide; however, the high cost and rarity of these noble metals are handicaps for their large-scale application [10]. In addition, there is a great deal of interest in using solar energy towards H₂ and H₂O₂ production, by employing photo/electroactive catalysts, which are able to absorb some of the solar radiation to assist electrolysis of water or oxygen reduction, further reducing the environmental impact of these processes. Despite that enormous efforts have been made in this topic [11], there are still only few efficient non-noble metal bifunctional photo/electrocatalysts [12–14] catalyzing both of the above reactions.

Single-atom catalysts have emerged as a promising alternative to noble-metal based state-of-the-art electrocatalysts due to their high atomic utilization efficiency as well as their extraordinary activity and selectivity [15]. In this context, metalloporphyrins, that are single-atom molecular catalysts, featuring a central metal atom strongly coordinated with four nitrogen atoms in the form of M-N₄ motifs [16, 17], have been employed extensively as photo/electrocatalysts for key electrochemical reactions, including WOR and ORR, due to their high extinction coefficient in the visible range and high chemical stability [18, 19]. The immobilization of single-atom molecular catalysts onto supports is highly desirable in heterogeneous catalysis, offering not only enhanced catalyst stability and recyclability but more importantly better accessibility of the reactants to single-atom active sites by preventing possible aggregation [20].

Two-dimensional molybdenum disulfide (MoS₂), an earth-abundant material, with a large surface-to-volume ratio, has received special scientific attention in photo/electrocatalytic applications thanks to its tunable electronic properties and intrinsic electrocatalytic activity [21–24]. Particularly, the octahedral coordination geometry of Mo in the 1T polymorph of MoS₂ rationalizes its participation in electrocatalysis by considering the inherent reduced

charge-transfer resistance [23]. On this basis, hybridization of MoS₂ with metalloporphyrins not only provides a favorable way for further improving WOR and/or ORR efficiency but also fully exploits the light harvesting properties of metalloporphyrins, en route the realization of novel multifunctional photo/electrocatalysts. To the best of our knowledge, there are only few reports on metalloporphyrin/transition metal dichalcogenide photo/electrocatalysts focused on HER [25–29], while on WOR and ORR remain unexplored.

The present work goes beyond the current state-of-the-art by enabling cationic modified MoS₂ nanosheets, electrostatically assembled with an anionic cobalt porphyrin (CoP), to efficiently perform as novel bifunctional photo/electrocatalyst toward water oxidation as well as ORR for selective H₂O₂ production. Markedly, our design strategy is based on flexibility and simplicity and relies on strong ion-pair interactions between an imidazolium-modified MoS₂ material and a carboxylated CoP. Importantly, the main reasons for choosing CoP as active component, nanointegrated within the modified MoS₂, are the following: (a) CoP is composed of earth-abundant, non-precious elements, (b) CoP has been proven to act as efficient homogeneous or heterogeneous single-atom molecular photo/electrocatalyst toward WOR [30–33] and ORR [34–38], and (c) mononuclear CoP catalyzes selectively ORR to H₂O₂ [39]. Needless to say, according to theoretical calculations the Co-N₄ motif in CoP possesses the optimal adsorption energy of *OOH intermediate for H₂O₂ production, among a series of single atom metal centers, including Mn, Fe, Cu, Ni, etc [40]. Taking advantage of the excellent photo/electrocatalytic properties of CoP, together with the intriguing electronic properties of MoS₂ nanosheets, the newly developed CoP/MoS₂ nanoensemble showed notable bifunctional electrocatalytic activity for water oxidation and selective H₂O₂ production in alkaline conditions, with significantly improved performance upon illumination. Remarkably, we refer an enhanced by 130% current density value and an 80 mV lower onset overpotential, *ca.* 1.575 V vs. reversible hydrogen electrode (RHE), toward WOR, under light irradiation conditions, while in the case of ORR its onset potential was shifted to 595 mV vs. RHE (only 105 mV overpotential for the 2e⁻ ORR pathway), followed by an 83% enhanced activity. At the same time, the achieved selectivity toward H₂O₂ formation was ranged between 95% and 98%. At this point, we would like to highlight that all the photo/electrocatalytic measurements were conducted on fluorine-doped tin oxide (FTO) coated glass electrodes, simulating perfectly the performance of the tested materials under practical application conditions (photo/electrochemical devices) by taking into account both diffusion phenomena (static electrodes, larger surfaces) and the intrinsic resistivity of

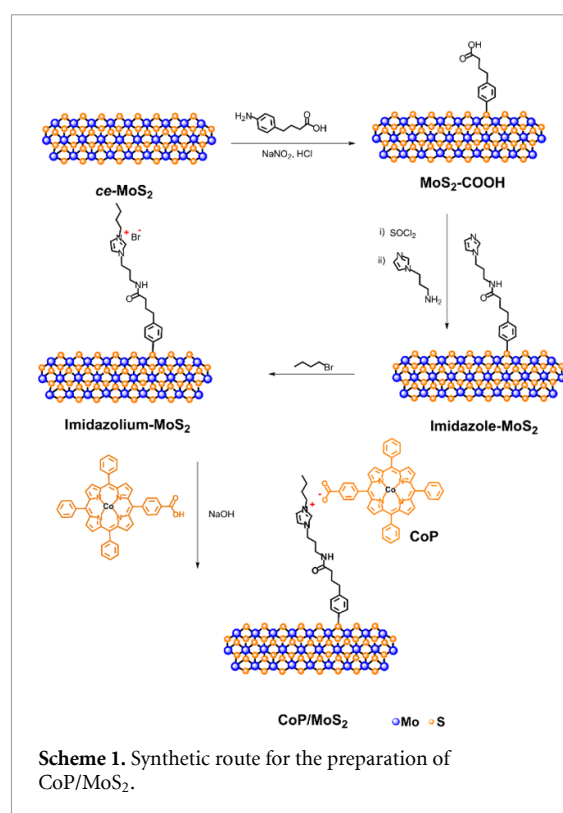
the FTO—coated glass substrates [41]. Overall, the CoP/MoS₂ ensemble was proved to be an efficient low-cost bifunctional photo/electrocatalyst, paving the way for sustainable industrial H₂ and selective H₂O₂ production.

2. Results and discussion

2.1. Material preparation and characteristics

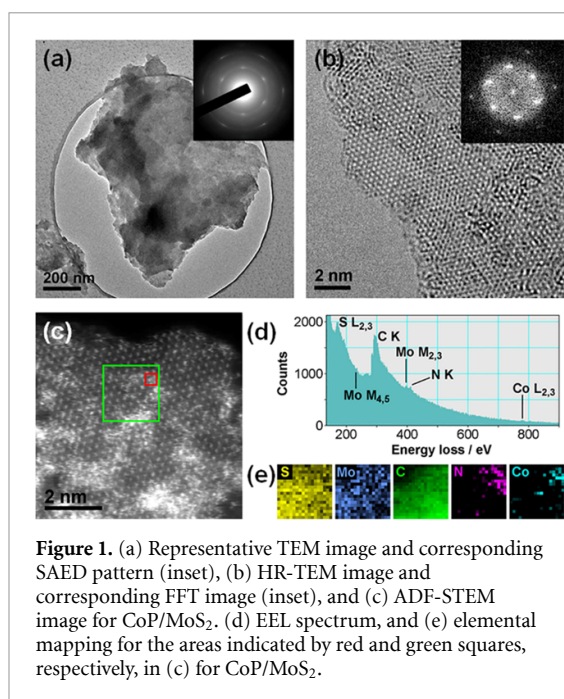
Starting point for the realization of the CoP/MoS₂ nanoensemble is, from one side, the exfoliation from the bulk of MoS₂, and from the other side, the cobalt mutilation of commercially available 5-(4-carboxyphenyl)-10,15,20-triphenylporphyrin. Considering that none of the two species, MoS₂ and metalated porphyrin, is charged, both of them need to be chemically modified in order to incorporate opposite charges to them that will effectively lead to the development of electrostatic interactions for tightly holding them together in the form of nanoensembles. The chemically exfoliated MoS₂ (*ce*-MoS₂) nanosheets were prepared upon treatment with *n*-BuLi, via lithium intercalation, of bulk MoS₂ [42–44]. Next, exfoliated MoS₂ was treated with the diazonium salt [45, 46] of 4-(4-aminophenyl)butyric acid, prepared *in-situ* at 0 °C, to obtain functionalized MoS₂ featuring carboxylic acid groups (MoS₂-COOH). Activation of the latter with thionyl chloride, followed by condensation with 1-(3-aminopropyl)imidazole, led to imidazole-MoS₂. Next, N-alkylation of the imidazole ring with 1-bromobutane yielded imidazolium-MoS₂, having bromide as counter anion, according to scheme 1. On a parallel synthetic route, 5-(4-carboxyphenyl)-10,15,20-triphenylporphyrin was first metalated and then deprotonated to afford anionic carboxylated CoP. Eventually, the CoP/MoS₂ nanoensemble was realized easy via a simple procedure, in which the bromide counter anion in imidazolium-MoS₂ was exchanged by the anionic CoP, allowing efficient integration of the photo/electrocatalytically active metalloporphyrin within the nanoensemble. In order to confirm the electrostatic interactions between the anionic CoP and the imidazolium-MoS₂, zeta potential measurements were performed. In more detail, the zeta potential for the nanoensemble CoP/MoS₂ was found to be neutral (i.e. −10 to +10 mV) contrasting the cases of anionic CoP and imidazolium-MoS₂, where it was found to be negative ca. -32.4 ± 9.45 mV and positive ca. $+26.4 \pm 9.13$ mV, respectively. For reference purposes, the corresponding anionic metal-free porphyrin, abbreviated as H₂P, was employed to similarly prepare H₂P/MoS₂, following the same ion exchange process.

According to the high-resolution and annular dark-field scanning transmission electron microscopy (HR-TEM and ADF-STEM, respectively) images shown in figures 1(a) and (b) and S1(a)–(b),



CoP/MoS₂ consists of oligo-layered MoS₂ sheets of varied size. Notably, no visible defects are observed at the hexagonal MoS₂ lattice, implying that the functionalization process does not affect the original nanostructure of the material. More interestingly, STEM imaging along with electron energy loss spectroscopy (EELS) chemical mapping (figures 1(c)–(e)) confirm the uniform and aggregation-free distribution of the CoP units onto the MoS₂ nanosheets. The latter finding is further supported by energy dispersive spectroscopy (EDS) mapping (figure S1(c)). Last, the reference material based on the metal-free porphyrin, H₂P/MoS₂, presented similar morphology to that of CoP/MoS₂ (figure S2).

Clear evidence for the successful formation of imidazolium-modified MoS₂-based material and the corresponding CoP/MoS₂ nanoensemble and H₂P/MoS₂ reference material came from detailed physicochemical characterization, comprising Raman and infrared spectroscopy (figures 2 and S3, respectively), x-ray diffraction (XRD) and x-ray photoelectron spectroscopy (XPS) (figures 3, S4 and S5), UV–Vis spectroscopy (figure S6), as well as thermogravimetric analysis (TGA) (figure S7) and electrochemical characterization (figure S8)—see supporting information for more details. Focusing on Raman spectroscopy analysis, we do not only get additional proof for the covalent functionalization of *ce*-MoS₂ by evaluating the 2LA(M)/A_{1g} intensity ratio [45, 46] (figure 2), but more importantly we gain useful insights on the polytype of MoS₂ during the functionalization process. It is known that in *ce*-MoS₂, as obtained via lithium intercalation as



in the current work, the metastable 1T octahedral phase irreversibly transforms to the 2H simply upon drying and aging [47]. In more detail, regarding the Raman spectrum of *ce*-MoS₂ (figure 2(a)), the signature phonon modes of 1T octahedral phase of MoS₂, namely J₁, J₂ and J₃ located at 154, 226 and 327 cm⁻¹, respectively, are clearly observed along with the presence of the E_{2g}¹ mode (~380 cm⁻¹), which is usually witnessed in 2H-MoS₂, indicating the co-existence of the metallic and the semiconducting phase within the *ce*-MoS₂ material [48–50]. Then, changes are evidently seen when comparing the Raman spectrum of *ce*-MoS₂ with the spectra belonging to functionalized MoS₂ materials. Interestingly, the A_{1g}/E_{2g}¹ intensity ratio was found decreased by 15%, while at the same time the relative intensity of J₁, J₂ and J₃ was lowered, implying that the functionalization process results in a partial transformation of 1T to 2H phase of MoS₂. At this point, it should be noted that although the structural changes occurred during functionalization, the metastable octahedral symmetry of Mo is significantly retained as the J₁, J₂, J₃ phonon modes of 1T-MoS₂ are still apparent. Interestingly, the co-existence of 1T and 2H phase at imidazolium-MoS₂ and consequently at the corresponding CoP/MoS₂ is highly desirable when considering their use in photo/electrocatalysis [51–53]. Needless to say, the 1T/2H mixed phase of MoS₂ benefits from the synergistic effect between the two phases and the enhanced stability of the metastable 1T phase within the nanoensembles [54]. Importantly, the metallic 1T phase of MoS₂ contributes to higher carrier mobility [54] along with enhanced catalytic performance for energy conversion applications [23, 55], while the semiconductive 2H phase is characterized by a moderate bandgap which is preferable in photocatalytic applications

[56–58]. Indeed, when an organic semiconductor (i.e. porphyrin) is attached to the 2H phase of MoS₂, a type II band alignment is expected to occur leading into efficient charge separation and transfer within the hybrid material [56, 57], which are essential for its photo/electrocatalytic properties. Moreover, a Schottky contact (metal–semiconductor junction) should be formed between the metallic 1T phase and the porphyrin unit [59–61]. Therefore, in the case of CoP/MoS₂ upon illumination, the photoexcited electrons generated in the porphyrin are readily injected into MoS₂ through the formation of a type II heterojunction or Schottky contact with the 2H and 1T polymorphs, respectively, and efficiently transferred at the interface with the aqueous solution, giving rise to the photo/electrochemical reaction [28, 62, 63]. Last, the successful functionalization of *ce*-MoS₂ was further confirmed by evaluating the intensity ratio of 2LA(M) (~450 cm⁻¹) to A_{1g} (404 cm⁻¹). Here, the 2LA(M)/A_{1g} value was found decreased for the functionalized materials MoS₂-COOH and imidazolium-MoS₂, implying the successful functionalization process. The latter observation was further confirmed through complementary Raman spectroscopy mapping assays, revealing an average intensity ratio 2LA(M)/A_{1g} of 0.95 and 0.97 for MoS₂-COOH and imidazolium-MoS₂, respectively versus 1.20 for *ce*-MoS₂, as presented in figures 2(b)–(d).

Similar conclusions regarding the MoS₂ phases of the studied materials and the changes occurred during the functionalization process were obtained by XRD and XPS analysis. In more detail, figure 3(a) shows the powder XRD patterns of *ce*-MoS₂ and imidazolium-MoS₂, suggesting that the metallic 1T phase is prevalent in both materials (for comparison, diffractogram of bulk 2H-MoS₂ is provided in figure S4(a)). Indeed, the typical (002) peak at 14.1° of the hexagonal 2H-MoS₂ polytype does not appear upon the chemical exfoliation procedure, while at the same time new peaks centered at 9.7° (001), 17° (010) and 42° (120) related to the 1T phase are emerged. In addition, in both *ce*-MoS₂ and imidazolium-MoS₂, the (200) peak at 56° is downshifted, compared to the corresponding (110) diffraction in 2H-MoS₂ at 60°, as the lattice parameter is expanded (3.21 Å in 1T-MoS₂ and 3.16 Å in 2H-MoS₂) [64, 65]. To determine the stoichiometric 1T:2H phase ratio in each material, XPS assays were carried out. The deconvoluted Mo 3d spectra of *ce*-MoS₂ and CoP/MoS₂ are depicted in figures 3(b) and (c), respectively, displaying notable differences from that belonging to 2H-MoS₂ (figure S4(b)), showing additional peaks with a shift to lower binding energy of ~1.0 eV, which corresponds to the 1T phase. Precisely, the doublet at ~228.4 and 231.5 eV is ascribed to 1T-MoS₂, while the doublet at ~229.6 and 232.7 eV is assigned to 2H-MoS₂. The additional doublets at ~230.5 and 233.6 eV as well as ~232.8 and 236.0 eV are associated with different oxidation states of Mo

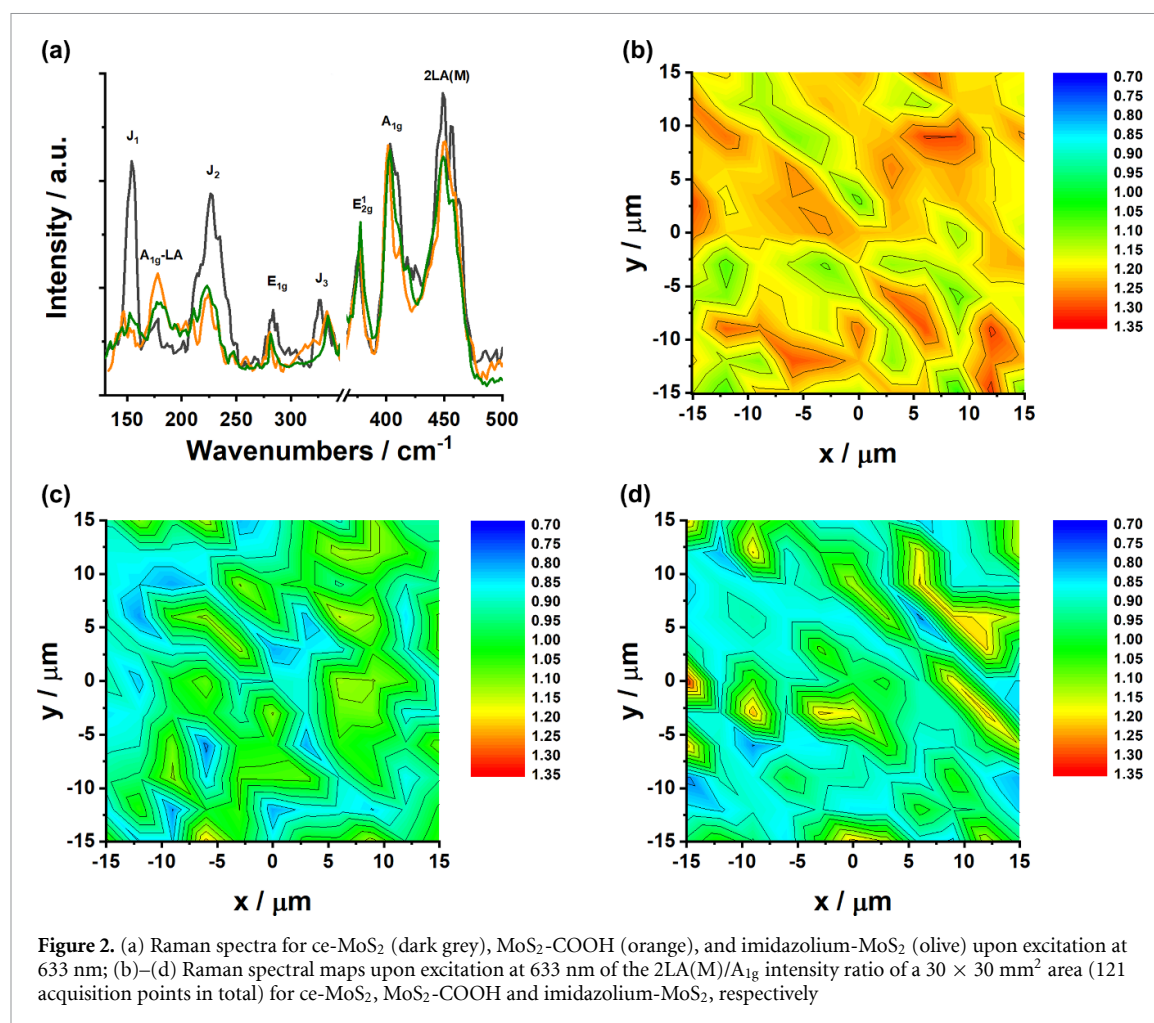


Figure 2. (a) Raman spectra for *ce*-MoS₂ (dark grey), MoS₂-COOH (orange), and imidazolium-MoS₂ (olive) upon excitation at 633 nm; (b)–(d) Raman spectral maps upon excitation at 633 nm of the 2LA(M)/A_{1g} intensity ratio of a 30 × 30 mm² area (121 acquisition points in total) for *ce*-MoS₂, MoS₂-COOH and imidazolium-MoS₂, respectively

(i.e. Mo_xS_y and MoO₃, respectively) [64, 66]. The stoichiometric 1T:2H ratio obtained from the fitted data in figures 3(b) and (c) is 2.4:1 and 1.7:1 in favor of the 1T phase, for *ce*-MoS₂ and CoP/MoS₂, respectively. The latter result suggests a slightly lower 1T content for the nanoensemble, providing additional proofs for the co-existence of both 1T and 2H phases at CoP/MoS₂. In order to understand the partial transformation of the 1T to 2H phase during the different steps of the functionalization procedure, we conducted XPS measurements in all the intermediate materials, namely, MoS₂-COOH, imidazole-MoS₂ and imidazolium-MoS₂ (figure S5). According to the results, the partial transformation of the 1T to 2H phase occurs during the preparation of the imidazole-MoS₂, probably due to the long residence of the MoS₂ nanosheets into the warm solution (for more details, see section 4.4).

2.2. Photo/electrocatalytic performance

The photo/electrocatalytic performance of CoP/MoS₂ toward water oxidation and ORR for H₂O₂ formation was examined in alkane electrolyte through linear sweep voltammetry (LSV) on a FTO coated glass electrode under dark and light irradiation conditions (500 W halogen lamp). Remarkably,

the use of the FTO set-up not only enable us to evaluate its photo/electrocatalytic activity but also simulates perfectly the practical conditions in photo/electrochemical devices. In the case of ORR, complementary electrocatalytic measurements on a rotating ring-disk electrode (RRDE) were carried out in order to assess the selectivity of the reaction toward H₂O₂. As reference systems in the assessment, CoP, H₂P, imidazolium-MoS₂ and H₂P/MoS₂ were employed.

2.2.1. WOR

The WOR photo/electrocatalytic activity of CoP/MoS₂ in N₂-saturated aqueous 0.1 M KOH as compared with that of the reference materials is displayed in figures 4 and S9. Under dark conditions, CoP/MoS₂ exhibited an activity remarkably higher than that of its unsupported CoP by requiring the smallest overpotential to commence the WOR *ca.* 1.654 V vs. RHE as well as the greatest current density at the whole potential range. It is also important to mention that the Co-free control materials, namely, H₂P/MoS₂, H₂P and imidazolium-MoS₂, showed a very poor WOR performance with an onset potential higher than 1.9 V vs. RHE. Similar results have been reported in the literature for different

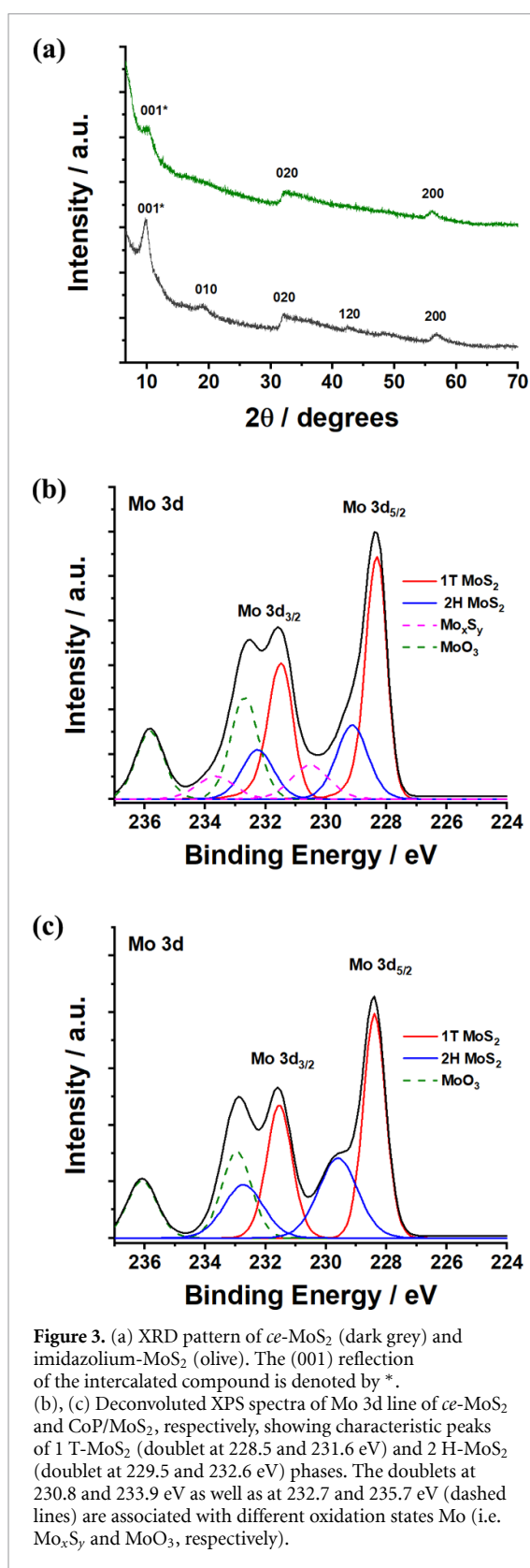


Figure 3. (a) XRD pattern of *ce*-MoS₂ (dark grey) and imidazolium-MoS₂ (olive). The (001) reflection of the intercalated compound is denoted by *. (b), (c) Deconvoluted XPS spectra of Mo 3d line of *ce*-MoS₂ and CoP/MoS₂, respectively, showing characteristic peaks of 1 T-MoS₂ (doublet at 228.5 and 231.6 eV) and 2 H-MoS₂ (doublet at 229.5 and 232.6 eV) phases. The doublets at 230.8 and 233.9 eV as well as at 232.7 and 235.7 eV (dashed lines) are associated with different oxidation states Mo (i.e. Mo_xS_y and MoO₃, respectively).

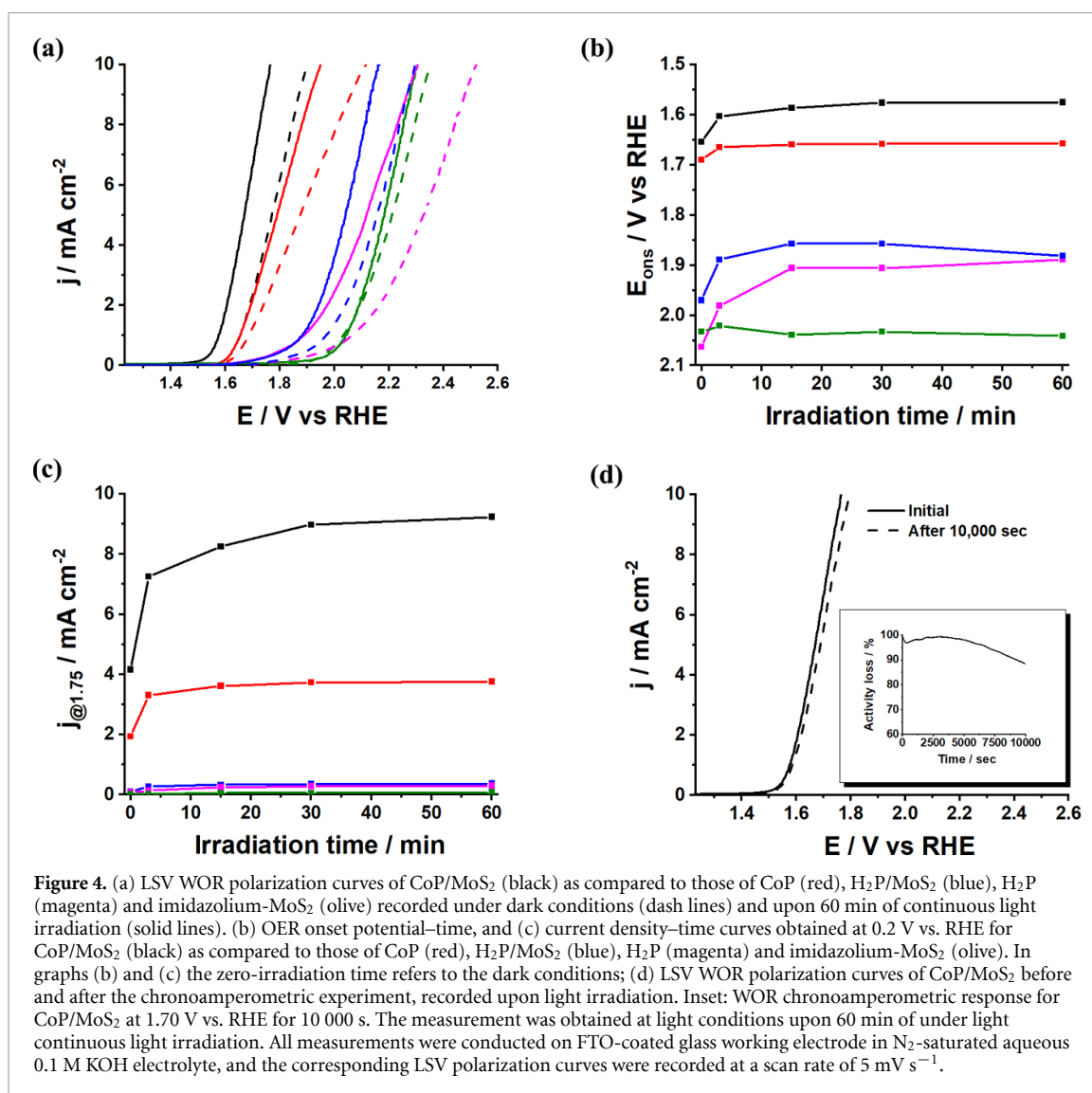
CoP—based catalysts whereas there are no reports on their photo/electrocatalytic performance (table S1) [30, 67]. To exemplify, CoP molecules intercalated into zirconium phosphate layers [67] presented an oxygen evolution onset potential of 1.6 V vs. RHE, being very close to our CoP/MoS₂ nanoensemble. Therefore, it is clear the advantageous role of Co atom

within CoP as active species toward WOR. Indeed, it has been demonstrated [30] that the WOR activity of Co-based porphyrins is ascribed to the easy formation of CoP-OH⁻ species, which further undergo a multi-electron transfer process and combine with H₂O or OH⁻ in the solution to form oxygen.

Upon illumination, CoP/MoS₂ ensemble exhibited enhanced current density and lower overpotential values almost immediately, ca. after 3 min, while within the 60 min testing period its performance continued to increase, reaching to a plateau after approximately 15–30 min (figures 4 and S9). Indeed, we found that the required overpotential to initiate WOR was significantly reduced by 19% to 345 mV (onset ca. 1.575 V vs. RHE), upon light irradiation. In addition, at a potential of 1.75 V vs. RHE, the current density reached at 4.1 and 9.3 mA cm⁻² in the absence and presence of light, respectively (130% activity boost). Importantly, the WOR activity of the unsupported CoP was also improved upon illumination; however this increment was weaker—only 7% decrease in the WOR onset overpotential and 80% in the recorded current density was recorded. The latter result indicates that MoS₂ substrate plays a critical role in the electrocatalytic and photo/electrocatalytic WOR performance of CoP/MoS₂ by increasing the conductivity of the film (1T phase characteristics) [23, 24] and allowing the full exploitation of the light harvesting properties of porphyrin through the strong electronic interactions developed between them and MoS₂ within the CoP/MoS₂ nanoensemble upon visible light irradiation [28, 56]. On the other hand, the observed performance enhancement in the presence of light for the free porphyrin CoP can be ascribed to the π - π stacking of the porphyrins in the films onto the FTO substrate, which allows long-standing charge-separation upon visible light irradiation [68, 69]. Analogous photoresponse was not observed in the case of imidazolium-MoS₂. Last, the inset of figure 4(d) depicts the chronoamperometric response of CoP/MoS₂ upon light illumination, revealing excellent long-term stability for WOR, showing only 12% activity loss after 10 000 s. On top of that, the LSV WOR polarization curve recorded after the chronoamperometric experiment (figure 4(d)) suggests an only 11 mV higher overpotential, further verifying the good WOR stability of CoP/MoS₂ under practical conditions.

2.2.2. ORR

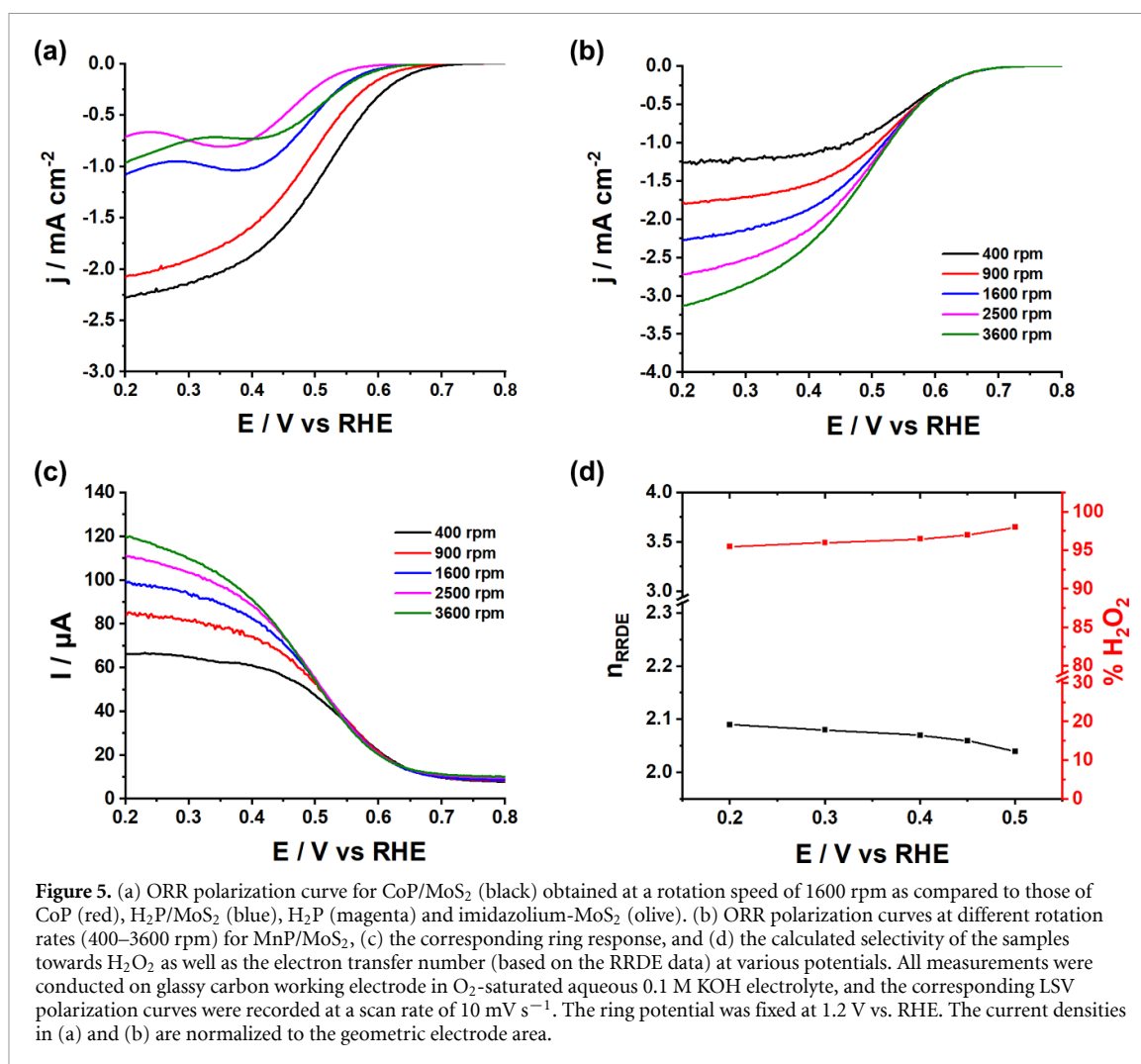
Overall, in alkaline electrolyte, ORR can proceed via two different reduction pathways, namely, the direct water production via a 4e⁻ reduction (O₂ + 2 H₂O + 4e⁻ → 4OH⁻, E^o = 1.230 V vs. RHE) and the 2e⁻ reduction route, which involves the formation of H₂O₂ (O₂ + H₂O + 2e⁻ → H₂O₂ + OH⁻, E^o = 0.700 V vs. RHE) [70, 71]. Therefore, before evaluating the ORR photo/electrocatalytic performance of CoP/MoS₂ ensemble, it is important



to scrutinize its selectivity toward H₂O₂. For that reason, hydrodynamic voltammetry assays were carried out on a RRDE in O₂-saturated 0.1 M KOH electrolyte. Figure 5(a) depicts the ORR polarization curve of CoP/MoS₂ ensemble obtained at a rotation rate of 1600 rpm as compared to those of CoP, H₂P/MoS₂, H₂P and imidazolium-MoS₂ references. As it can be seen, CoP/MoS₂ clearly presented the optimum performance among the tested catalysts, with a low overpotential value for the 2e⁻ ORR pathway of 27 mV ($E_{\text{ons}} = 673$ mV vs. RHE), followed by the unsupported CoP ($E_{\text{ons}} = 641$ mV vs. RHE). Figures 5(b) and (c) displays the disk and ring response for CoP/MoS₂ obtained at different rotation speeds in the range of 400–3600 rpm. Significant ring currents were recorded as a result of H₂O₂ generation. The H₂O₂ yield was plotted as a function of applied potential and it was calculated to be between 95% and 98% as shown in figure 5(d). Such high product selectivity toward H₂O₂ renders CoP/MoS₂ ideal for use in H₂O₂ production industry and can be mainly attributed to the absence of aggregations, as

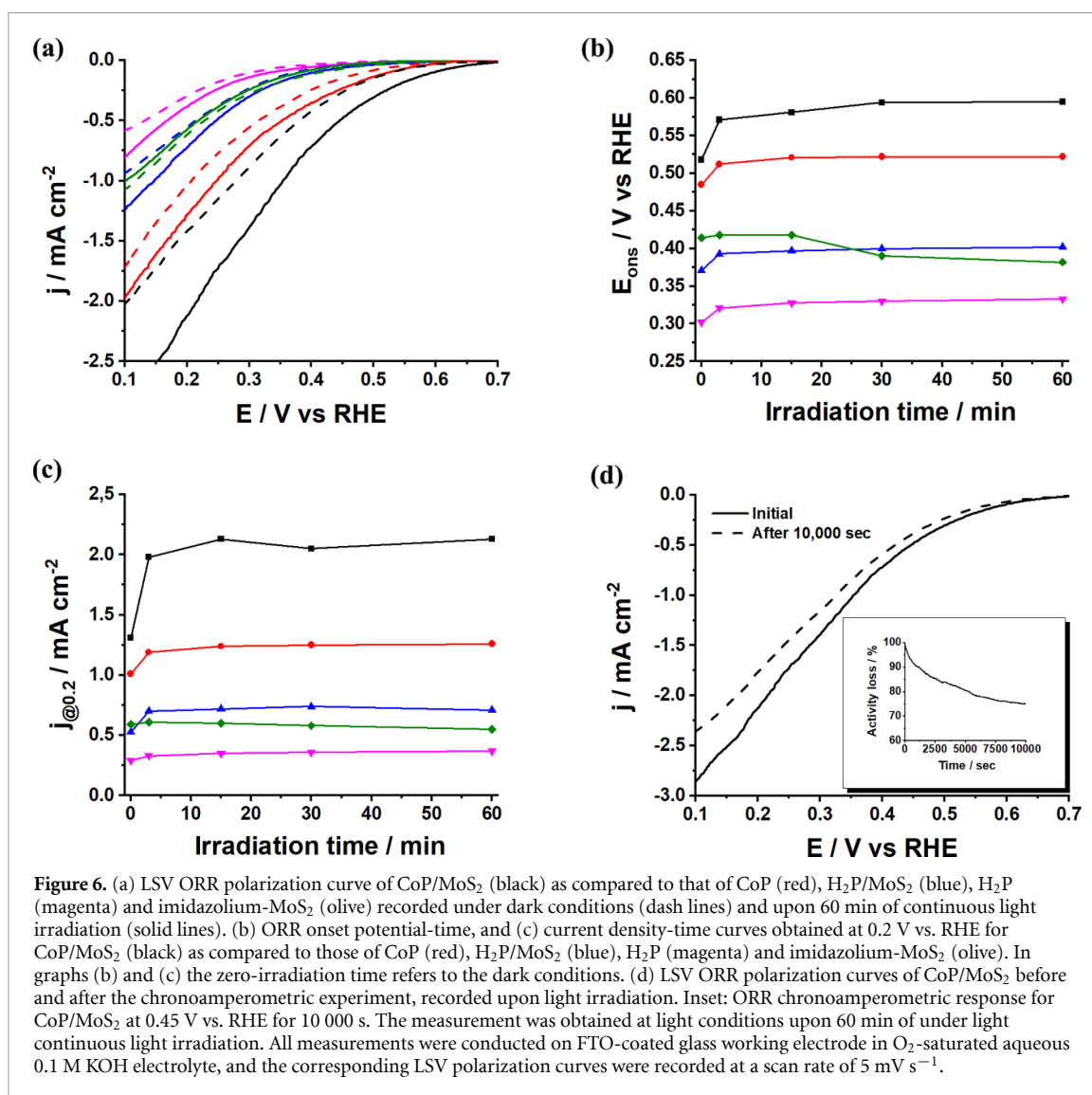
proved by EELS mapping. Interestingly, it has been demonstrated that aggregation of CoPs results in supramolecular arrangement of cobalt centers, which catalyze the 4e⁻ pathway oxygen reduction into water and thus significant drop on the catalyst selectivity toward H₂O₂ (table S2) [35, 39]. For instance, Sonkar *et al* [34] investigated the H₂O₂ selectivity of CoP/ multi-walled carbon nanotubes ensembles and found improved ORR activities in terms of onset potential but limited H₂O₂ selectivity in alkaline environment. These findings highlight the advantages of immobilizing CoP onto MoS₂ surface via electrostatical integration within the intra-nanoensemble, which is highly essential for preventing formation of supramolecular cobalt active sites, enabling to exploit the benefits arising from the single atom molecular catalyst.

Next, we investigated the ORR photo/electrocatalytic performance of CoP/MoS₂ in O₂-saturated aqueous 0.1 M KOH and compared it with that of the reference materials. Similar to the case of WOR, CoP/MoS₂ revealed the optimum ORR activity, in



both absence and presence of light irradiation, as shown in figures 6 and S10. More precisely, under dark conditions, CoP/MoS₂ surpassed both the unsupported CoP and its cobalt-free counterpart H₂P/MoS₂ by manifesting an ORR onset potential of 518 mV vs. RHE, which is 33 and 147 mV more positive than that of CoP and H₂P/MoS₂, respectively. In addition, the current density at 0.2 V vs. RHE for CoP/MoS₂ reached at 1.32 mA cm⁻², being 31% and 2.5 times higher over that of CoP and H₂P/MoS₂, respectively. Therefore, the improved ORR activity of CoP/MoS₂ can be ascribed to the enhanced conductivity offered by the 1T phase of MoS₂ [23, 24] and more importantly to the intrinsic ORR catalytic activity of the Co atom of CoP. Needless to say, mononuclear Co-macrocycles are considered to be ideal catalysts for the reduction of molecular oxygen toward the formation of H₂O₂ [72, 73]. Notably, upon light irradiation, CoP/MoS₂ continue to outperform the reference materials, demonstrating a significant enhancement of its initial ORR activity. Indeed, the generated photocurrent at 0.2 V vs. RHE for CoP/MoS₂ was found to be increased by 62% (2.10 mA cm⁻²), while its ORR onset potential was registered at 595 mV vs. RHE, being 77 mV

more positive compared to the value obtained under dark conditions. Analogous performance improvement was also observed for H₂P/MoS₂, however, the increment was much smaller for the unsupported porphyrins, CoP and H₂P. Remarkably, the later result is consistent with our observations in the case of WOR, further proving the strong synergistic effect between porphyrin and MoS₂, within CoP/MoS₂, in the presence of light, which due to the formation of a type II heterojunction and/or Schottky contact is responsible for the excellent ORR photo/electrocatalytic performance of the nanoensemble [28, 56, 63]. At this point, it has to be acknowledged that the different LSV profile along with the higher overpotential by 130 ± 20 mV obtained on the FTO-coated electrode compared to those on the RRDE electrode (figure 5(a)) is well justified by considering the elimination of the diffusion phenomena through the drastic convection achieved by the high-speed rotation as well as the intrinsic resistivity of the FTO. However, the use of the stationary FTO-coated electrode in the photo/electrocatalytic experiments does not affect the H₂O₂ selectivity that determined using the RRDE setup. Last but not least, chronoamperometry tests of CoP/MoS₂ suggested good stability for

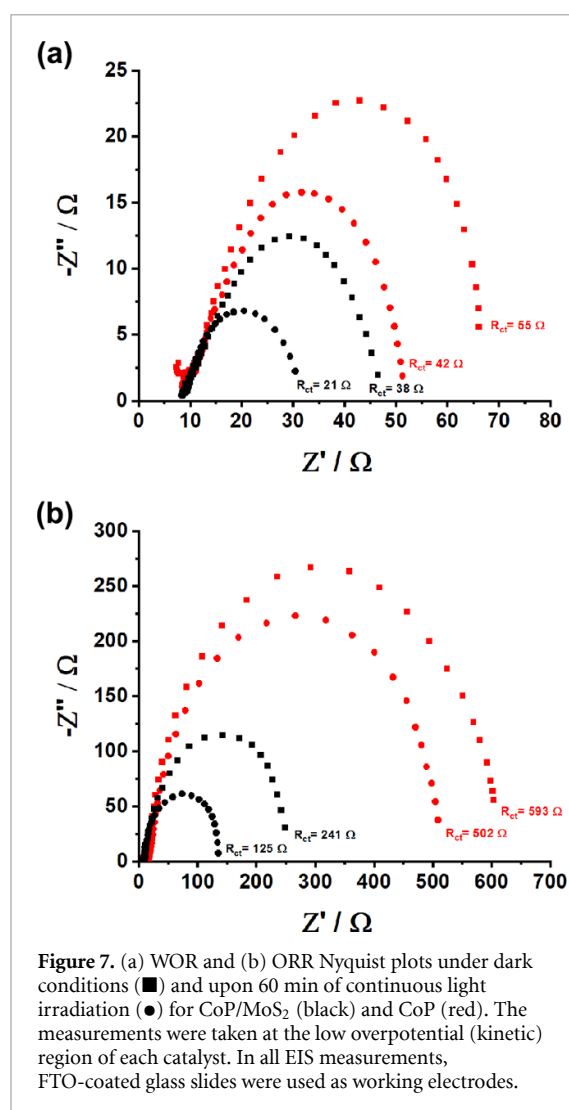


ORR under light conditions by retaining the 75% of its initial value after 10 000 s, as shown in the inset of figure 6(d). At the same time, the LSV polarization curve recorded after the chronoamperometric experiment (figure 6(d)) exhibits an increased ORR overpotential by 25 mV ($E_{\text{ons}} = 570$ mV).

2.2.3. Electrochemical impedance spectroscopy (EIS)

EIS was employed to study the charge transfer at the electrode/ electrolyte interface under WOR and ORR conditions, in both absence and presence of light irradiation, for CoP/MoS₂ and CoP electrodes, and therefore to provide useful insights on the reaction kinetics. In all cases, the EIS measurements were performed at the low overpotential (kinetic) region and the obtained data were fitted to Randles circuit (figure S11) [74]. The Nyquist plots of CoP/MoS₂ and CoP, representing negative of the imaginary versus the real part of the impedance under WOR and ORR conditions, are shown in figures 7(a) and (b), respectively. Briefly, the diameter of the semicircle of the Nyquist plot relates to the electron

transfer process from the electrode surface into the electrolyte solution and the smaller the semicircle implies the less the charge transfer resistance (R_{ct}). In absence of light illumination, the semicircle of CoP/MoS₂ revealed a smaller diameter by 30% for WOR conditions and 60% for ORR than that of the CoP, attributed to the high conductance derived by the presence of the 1T phase of MoS₂ substrate. This result further justifies the boosted electrocatalytic activities of our CoP/MoS₂ nanoensemble compared to those of the intact molecular porphyrin species. Upon light illumination, the R_{ct} value of the CoP/MoS₂ electrode was further decreased by 45%–48%, under both WOR and ORR conditions, implying that the presence of light favors the interfacial charge transfer process. In more detail, the efficient intra-hybrid charge transfer upon light irradiation due to the formation of type-II heterojunction or Schottky contact enhances the charge transfer process at the electrode/electrolyte interface and therefore leads to the rapid consumption of the photo-generated electrons/holes by the reaction, quenching



the charge recombination and boosting the reduction/oxidation kinetics [75, 76]. Needless to mention, the CoP based electrode exhibited also reduced R_{ct} values in presence of light; however, the drop-off was ranged between 15% and 20% being much lower when compared with that observed for the hybrid electrode. Here, the lower R_{ct} values are attributed to the π - π stacking of the porphyrin in the films which permits the long-standing charge-separation upon visible light irradiation [68, 69]. Overall, the EIS results are consistent with the observed enhanced catalytic photo/electrocatalytic activity of the CoP/MoS₂ towards WOR and ORR and provide us additional proofs for the beneficial role of the 1T/2H mixed phase of MoS₂ as support for the porphyrin moieties.

3. Conclusion

In summary, we took the advantage of the versatile catalytic and light harvesting properties of a CoP as well as the intriguing electronic properties of MoS₂ sheets to realize an earth-abundant single-atom bifunctional photo/electrocatalyst, namely CoP/MoS₂, for water oxidation and H₂O₂ production

in basic conditions. Our approach relies on strong ion-pair interactions between the imidazolium-based MoS₂ material and the carboxylated CoP, which prevent possible aggregation of cobalt atoms and thus ensure the better accessibility of the reactants to single-atom active sites. Complementary spectroscopic techniques, along with TGA and HR-TEM and ADF-STEM imaging and EELS chemical analysis not only verified the successful formation of the CoP/MoS₂ nanoensemble but also allowed to confirm the uniform and aggregation-free distribution of CoP moieties on the MoS₂ surface. The co-existence of 1T and 2H polymorphs at the modified MoS₂, as proved by Raman and XPS analysis, benefits the overall photo/electrocatalytic performance of CoP/MoS₂ by offering improved electrical conductivity and intrinsic electrocatalytic activities, especially toward HER (1T phase), as well as enhanced intraensemble electronic interactions leading to efficient charge separation and transfer properties (2H phase), as proved by the EIS data. As a result, CoP/MoS₂ exhibited much greater electrocatalytic activities toward WOR and ORR compared to its unsupported counterpart and more importantly significantly lower overpotential values along with enhanced current densities in the whole potential range upon light illumination. In addition, a 95%–98% selectivity of CoP/MoS₂ toward H₂O₂ formation, rendering it ideal for industrial application, was registered. Overall, these findings pave the way for future designs of novel nonprecious bifunctional photo/electrocatalysts for the sustainable production of H₂ via water electrolysis and the selective H₂O₂ formation via the two-electron reduction of oxygen.

4. Experimental section

4.1. Materials

MoS₂ powder (particle size $\sim 6 \mu\text{m}$, max. $40 \mu\text{m}$), 4-(4-aminophenyl) butyric acid (95%), 1-(3-aminopropyl)imidazole (98%), 1-bromobutane (99%), (FTO) coated glass slides (surface resistivity $\sim 7 \Omega \text{ sq}^{-1}$), thionyl chloride (97%), *n*-BuLi (2.5 M in hexanes), were purchased from Sigma-Aldrich and were used as received. 5-(4-carboxyphenyl)-10,15,20-triphenylporphyrin was purchased from PorphChem.

4.2. Preparation of *ce*-MoS₂

Exfoliated MoS₂ was prepared by Li-intercalation of bulk MoS₂. Initially, MoS₂ powder was dried at 150 °C under vacuum overnight previous to use. Briefly, under N₂ atmosphere 2.5 M *n*-BuLi (5 ml, 12.5 mmol) was added to bulk MoS₂ (500 mg, 3.13 mmol) and the resultant mixture was stirred at room temperature for 48 h. After that period, the intercalated MoS₂ was let to settle and the supernatant *n*-BuLi solution was carefully removed under N₂ atmosphere. Next, dry hexane (10 ml) was added

under N₂, the resultant dispersion was stirred for 10 min, was let to settle and then the supernatant was carefully removed under N₂. This procedure was repeated three times in total, to ensure the elimination of the excess of *n*-BuLi. The residual intercalated MoS₂ slurry was dispersed in distilled water (400 ml) and tip sonicated for 3 h (keeping the temperature below 30 °C with the aid of ice bath). Finally, the black suspension was let to settle for 12 h, the top 2/3 were collected and stored in a sealed flask. The concentration of the exfoliated MoS₂ suspension was 1 mg ml⁻¹.

4.3. Preparation of MoS₂-COOH

Basal plane functionalization of *ce*-MoS₂ featuring carboxylic groups (MoS₂-COOH) was achieved through an *in-situ* diazotization reaction. First, the diazonium salt was prepared by dissolving 4-(4-aminophenyl)butyric acid (225 mg, 1.25 mmol) in 2:1 v/v water/ethanol (30 ml) through the addition of concentrated HCl (105 μl, 1.25 mmol). Then, NaNO₂ (87 mg, 1.25 mmol) and concentrated HCl (105 μl, 1.25 mmol) were added slowly and the resultant suspension was allowed to stir at ice-cold temperature for 45 min until the color turns to deep yellow indicating the diazotization reaction. Next, 100 ml of a freshly prepared aqueous exfoliated MoS₂ (1 mg ml⁻¹) was added dropwise to the diazonium salt solution and the mixture allowed to reach room temperature overnight under vigorous stirring. Finally, the reaction mixture was filtered through a 0.2 μm PTFE membrane filter and washed with copious amounts of acetone and water to yield after vacuum dryness 105 mg of MoS₂-COOH as black solid.

4.4. Preparation of imidazole-modified MoS₂

First, MoS₂-COOH (40 mg) was treated with thionyl chloride (20 ml) at 65 °C overnight under an inert atmosphere to activate the carboxylic units. Next, the excess thionyl chloride was evaporated under reduced pressure and the remaining solid was carefully washed with anhydrous tetrahydrofuran under nitrogen. The as-produced acyl-chlorinated MoS₂ (40 mg) was dispersed in dry tetrahydrofuran (20 ml) followed by the addition of 250 μl of 1-(3-aminopropyl)imidazole and the reaction mixture was refluxed for 24 h. The resulting suspension was filtered through a 0.2 μm PTFE membrane filter and the solid residue was extensively washed with dichloromethane to remove organic residues before being dried under vacuum to afford 42 mg of imidazole-modified MoS₂ as black powder.

4.5. Preparation of [Br⁻] imidazolium-modified MoS₂

Imidazole-modified MoS₂ (35 mg) was treated with 1-bromobutane (7 ml) at 90 °C for 24 h. Then, the reaction mixture was filtered over a 0.2 μm PTFE

membrane filter and the solid residue was extensively washed with tetrahydrofuran (200 ml), 1N HCl (100 ml), saturated NaHCO₃ (100 ml) and deionized water (300 ml) and dried under vacuum to afford 40 mg of [Br⁻] imidazolium-modified MoS₂ as black powder.

4.6. Synthesis of 5-(4-carboxyphenyl)-10,15,20-triphenylporphyrin Co(II)

5-(4-carboxyphenyl)-10,15,20-triphenylporphyrin (10 mg, 0.015 mmol) and CoCl₂ (54 mg, 0.22 mmol) were dissolved in DMF (5 ml) and the solution was heated to reflux for 4 h. Then, the solvent was distilled under reduced pressure. The residue was dissolved in CH₂Cl₂ together with two drops of methanol and washed with water. The organic layer was dried over Na₂SO₄, filtered and concentrated to dryness. Column chromatography (SiO₂, CH₂Cl₂/MeOH, 96:4) and reprecipitation of the product with CH₂Cl₂ and cold hexane afforded the entitled CoP as dark red-brown solid (9 mg, 83%). ¹H-NMR signals were broad due to the presence of paramagnetic Co(II). UV-Vis (tetrahydrofuran (THF)): λ (ε, mM⁻¹ cm⁻¹) = 416 (22.3), 532 (1.4), FT-IR: $\tilde{\nu}$ = 1691 (C=O carboxylic), 1604 (C=C), 1354 (C-N), 1070 (C-H), 704 (N-H) cm⁻¹ (porphyrin core vibrations).

4.7. Preparation of CoP/MoS₂

CoP (1.8 mg, 0.0025 mmol) was dissolved in THF (1 ml) and 0.1 M NaOH (180 μl, 6 eq.) were added. At first, 1 eq. of 0.1 M NaOH was added and the IR spectrum was recorded. It was found that 6 eq. in total were required for the fully conversion of CoP to the corresponding carboxylate sodium salt. Then an equivalent amount of [Br⁻] imidazolium-modified MoS₂ (3 mg, 0.0025 mmol) dispersed in H₂O (1 ml), was bath sonicated for 5 min and added in the CoP solution. The resulting solution was bath sonicated for another 5 min and left to stir overnight at room temperature. The resultant CoP/MoS₂ nanonensemble was kept as dispersion under stirring (concentration of 2.5 mg ml⁻¹). The reference material H₂P/MoS₂ was prepared following the same procedure using the corresponding carboxylated free porphyrin (1.65 mg, 0.0025 mmol), respectively.

4.8. Physical characterization

STEM combined with EDS and EELS were performed using a JEOL JEM-2100F microscope equipped with a couple of JEOL Centurio EDS detectors and a Gatan Quantum electron spectrometer at an electron accelerating voltage of 60 kV. FT IR spectra in the region of 550–4000 cm⁻¹ were obtained on a Fourier transform IR spectrometer (Equinox 55 from Bruker Optics) equipped with a single reflection diamond attenuated-total-reflectance accessory (DuraSamp1IR II by SensIR Technologies). Micro-Raman scattering measurements were performed in

the backscattering geometry using a RENISHAW inVia Raman microscope equipped with a charged-coupled device (CCD) camera and a Leica microscope. 2400 lines mm^{-1} grating (633 nm) were used, providing a spectral resolution of $\pm 1 \text{ cm}^{-1}$. As an excitation source He/Ne laser (633 nm) was used. Measurements were taken with 10 s of exposure times and laser power $\sim 0.3 \text{ mW cm}^{-2}$ to prevent overheating of the samples. The laser spot was focused on the sample surface using a long working distance $50\times$ (L50) objective. Raman spectra were collected on numerous spots (at least 10 mappings with 121 acquisition points each in a $30 \times 30 \text{ mm}^2$ area) on the sample and recorded with a Peltier cooled CCD camera. The data were collected and analyzed with Renishaw Wire and Origin software. Powder XRD patterns were collected on a PANalytical X'pert diffractometer (Cu-K α , $\lambda = 1.5406 \text{ \AA}$) with 45 kV and 40 mA at ambient temperature, using a continuous mode in the 2θ angular range of 5° to 70° with a scan speed of $0.0279^\circ \text{ s}^{-1}$. XPS was performed on a Kratos axis ultradelay line detector electron spectrometer using a monochromatic Al-K α source operated at 150 W. The analysis area of the spectrometer was $0.3 \times 0.7 \text{ mm}^2$. Binding energy scale of the spectrometer was calibrated using ISO standard 15472:2010 SCA-XPS-Calibration of energy scale [77]. Accuracy in binding energy (BE) position determination was 0.1 eV and in atomic ratios calculations better than 10%. TGA was performed using a Q500 V20.2 Build 27 instrument by TA in a nitrogen inert atmosphere. Steady state UV-vis electronic absorption spectra were recorded on a Perkin-Elmer (Lambda 19) UV-vis-NIR spectrophotometer.

4.9. Electrochemical and photo/electrochemical measurements

All electrochemical measurements were carried out using Autolab potentiostat/galvanostat PGSTAT128N (Metrohm Autolab) equipped with a dual mode bipotentiostat (BA module), which was controlled by NOVA 2.0 software.

4.9.1. Cyclic and square wave voltammetry experiments

Cyclic and square wave voltammetry experiments were carried out in dry and deoxygenated orthodichlorobenzene using a platinum working electrode (1 mm in diameter) and platinum wires were used as counter and pseudo-reference electrodes (Fc/Fc $^+$ as an internal reference) in 0.1 M TBAPF $_6$ as the supporting electrolyte.

4.9.2. RRDE measurements

RRDE measurements for ORR were conducted in a standard three compartment electrochemical cell using a RRDE setup from Metrohm Autolab consisted of a Teflon embedded glassy carbon disk/Pt ring rotating assembly (5 mm electrode disk diameter, 375 μm

electrode gap, collection efficiency $N = 0.249$). As the counter electrode, a platinum wire was used and as the reference electrode an Hg/HgO (0.1 M KOH) electrode was placed into the Luggin capillary. For the preparation of the working electrode, first an aliquot of 5 μl containing 2.5 mg ml^{-1} of each electrocatalyst dispersed in a mixture of 1:1 THF and water was deposited onto the working electrode and let it to dry under vacuum. Then, another aliquot of 5 μl containing water, isopropanol, and 5% Nafion ($v/v/v = 4:1:0.02$) was casted onto the catalyst modified working electrode surface and let it to dry under vacuum. The electrochemical measurements were carried out in O $_2$ -saturated 0.1 M KOH solution at room temperature at a scan rate (ν) of 10 mV s^{-1} . The n value and the percentage (%) of the produced H $_2$ O $_2$ can be determined using the following equations:

$$n = 4I_{\text{Disk}} / (I_{\text{Disk}} + I_{\text{Ring}}/N) \quad (1)$$

$$\%H_2O_2 = (200I_{\text{Ring}}/N) / (I_{\text{Disk}} + I_{\text{Ring}}/N) \quad (2)$$

where, I_{disk} is the current of the disk electrode, I_{ring} is the current of the ring electrode, and N is the collection efficiency of the Pt ring, which was provided as 0.249 by the manufacturer.

4.9.3. Photo/electrochemical experiments

For the preparation of working electrodes, all materials were deposited on 1 cm^2 conductive FTO coated glass slides (surface resistivity $\sim 7 \Omega \text{ Sq}^{-1}$) from solution (100 μl containing 2.5 mg ml^{-1} of each electrocatalyst dispersed in a mixture of 1:1 THF and water), and then dried under nitrogen. Then, another aliquot of 100 μl containing water, isopropanol, and 5% Nafion ($v/v/v = 4:1:0.02$) was casted onto the catalyst modified FTO surface and let it to dry under vacuum. Before deposition, all FTO-coated glass substrates (geometric area of 1 cm^2) were cleaned by a standard procedure in ultrasonic bath in detergent, deionized water and isopropanol for 15 min each and finally dried under a nitrogen flow. As counter electrode, a platinum wire was used and as reference an Hg/HgO (0.1 M KOH) electrode was placed into the Luggin capillary. As a light source, a conventional linear (118 mm) 500 W halogen lamp was used. The photo-electrochemical WOR measurements were realized in N $_2$ -saturated aqueous 0.1 M KOH electrolyte while the photo-electrochemical ORR measurements in O $_2$ -saturated aqueous 0.1 M KOH. LSV polarization curves were recorded with a scan rate of 5 mV s^{-1} . The measured potentials were converted to the RHE using the Nernst equation ($E_{\text{RHE}} = E_{\text{Hg/HgO}} + 0.165 + 0.059 \text{ pH}$). Chronoamperometric measurements were probed at 1.70 V vs. RHE (WOR) and 0.45 V vs. RHE (ORR) for 10 000 s. EIS measurements were conducted in the frequency range between 10^{-1} and 10^5 Hz with a AC amplitude of 0.01 V at applied DC potentials being at

the low overpotential region (typically, EIS measurements were performed at 10 mV higher overpotential than the onset potential of each material). Analysis of the impedance data was carried out by the NOVA 2.0 software.

Data availability statement

All data that support the findings of this study are included within the article (and any supplementary files).

Acknowledgments

This research is co-financed by Greece and the European Union (European Social Fund—ESF) through the Operational Programme ‘Human Resources Development, Education and Lifelong Learning’ in the context of the project ‘Reinforcement of Postdoctoral Researchers—2nd Cycle’ (MIS-5033021), implemented by the State Scholarships Foundation (IKY). Y S and K S acknowledge JSPS KAKENHI (Grant No. JP22K04886) and JST-CREST (Grant No. JPMJCR20B1), respectively, for financial support. XRD and XPS measurements were supported by Umeå University facilities. The authors wish to thank Dr Andrey Shchukarev for XPS measurements and analysis. D K P and C S contributed equally to this work.

ORCID iDs

Dimitrios K Perivoliotis  <https://orcid.org/0000-0002-3934-2062>

Christina Stangel  <https://orcid.org/0000-0003-4822-9317>

Yuta Sato  <https://orcid.org/0000-0002-4231-6287>

Kazu Suenaga  <https://orcid.org/0000-0002-6107-1123>

Nikos Tagmatarchis  <https://orcid.org/0000-0001-7590-4635>

References

- [1] Møller K T, Jensen T R, Akiba E and Li H-W 2017 *Prog. Nat. Sci.* **27** 34–40
- [2] Suryanto B H R, Wang Y, Hocking R K, Adamson W and Zhao C 2019 *Nat. Commun.* **10** 5599
- [3] Mase K, Yoneda M, Yamada Y and Fukuzumi S 2016 *Nat. Commun.* **7** 11470
- [4] Zhao D, Zhuang Z, Cao X, Zhang C, Peng Q, Chen C and Li Y 2020 *Chem. Soc. Rev.* **49** 2215–64
- [5] Fukuzumi S, Yamada Y and Karlin K D 2021 *Electrochim. Acta* **82** 493–511
- [6] Stamenkovic V R, Strmcnik D, Lopes P P and Markovic N M 2017 *Nat. Mater.* **16** 57–69
- [7] Lewis N S and Nocera D G 2006 *Proc. Natl Acad. Sci.* **103** 15729
- [8] Chia X and Pumera M 2018 *Nat. Catal.* **1** 909–21
- [9] Seh Z W, Kibsgaard J, Dickens C F, Chorkendorff I, Nørskov J K and Jaramillo T F 2017 *Science* **355** eaad4998
- [10] Lee Y, Suntivich J, May K J, Perry E E and Shao-Horn Y 2012 *J. Phys. Chem. Lett.* **3** 399–404
- [11] Roger I, Shipman M A and Symes M D 2017 *Nat. Rev. Chem.* **1** 0003
- [12] Jia Y, Zhang L, Du A, Gao G, Chen J, Yan X, Brown C L and Yao X 2016 *Adv. Mater.* **28** 9532–8
- [13] Amiin I S, Pu Z, Liu X, Owusu K A, Monestel H G R, Boakye F O, Zhang H and Mu S 2017 *Adv. Funct. Mater.* **27** 1702300
- [14] Jiang R, Baker D R, Tran D T, Li J, Leff A C and Zhang S S 2020 *ACS Appl. Nano Mater.* **3** 7119–29
- [15] Zang W, Kou Z, Pennycook S J and Wang J 2020 *Adv. Energy Mater.* **10** 1903181
- [16] Sun S, Yang X, Li S, Chen X, Li K, Lv J, Wang W, Cheng D, Wang Y-H and Zang H-Y 2021 *Catal. Sci. Technol.* **11** 2589–96
- [17] Yang X et al 2021 *Appl. Catal. B* **285** 119794
- [18] Natali M, Luisa A, Iengo E and Scandola F 2014 *Chem. Commun.* **50** 1842–4
- [19] Perivoliotis D K, Sato Y, Suenaga K and Tagmatarchis N 2020 *Nanoscale* **12** 18278–88
- [20] Hu X-M, Pedersen S U and Daasbjerg K 2019 *Curr. Opin. Electrochem.* **15** 148–54
- [21] Voiry D, Shin H S, Loh K P and Chhowalla M 2018 *Nat. Rev. Chem.* **2** 0105
- [22] Voiry D, Salehi M, Silva R, Fujita T, Chen M, Asefa T, Shenoy V B, Eda G and Chhowalla M 2013 *Nano Lett.* **13** 6222–7
- [23] Lukowski M A, Daniel A S, Meng F, Forticaux A, Li L and Jin S 2013 *J. Am. Chem. Soc.* **135** 10274–7
- [24] Yin Y et al 2016 *J. Am. Chem. Soc.* **138** 7965–72
- [25] Yuan Y-J, Chen D, Zhong J, Yang L-X, Wang -J-J, Yu Z-T and Zou Z-G 2017 *J. Phys. Chem. C* **121** 24452–62
- [26] Yuan Y et al 2015 *Chem. Eng. J.* **275** 8–16
- [27] Yuan Y-J, Tu J-R, Ye Z-J, Lu H-W, Ji Z-G, Hu B, Li Y-H, Cao D-P, Yu Z-T and Zou Z-G 2015 *Dyes Pigm.* **123** 285–92
- [28] Blanco M, Lunardon M, Bortoli M, Mosconi D, Girardi L, Orian L, Agnoli S and Granozzi G 2020 *J. Mater. Chem. A* **8** 11019–30
- [29] Kwon I S, Kwak I H, Abbas H G, Seo H W, Seo J, Park K, Park J and Kang H S 2019 *Nanoscale* **11** 3780–5
- [30] Wang X, Cai Z-F, Wang D and Wan L-J 2019 *J. Am. Chem. Soc.* **141** 7665–9
- [31] Liu B, Li J, Wu H-L, Liu W-Q, Jiang X, Li Z-J, Chen B, Tung C-H and Wu L-Z 2016 *ACS Appl. Mater. Interfaces* **8** 18577–83
- [32] Sun Z, Li J, Zheng H, Liu X, Ye S and Du P 2015 *Int. J. Hydrog. Energy* **40** 6538–45
- [33] Wang D and Groves J T 2013 *Proc. Natl Acad. Sci.* **110** 15579
- [34] Sonkar P K, Prakash K, Yadav M, Ganesan V, Sankar M, Gupta R and Yadav D K 2017 *J. Mater. Chem. A* **5** 6263–76
- [35] Liu Y, Zhou G, Zhang Z, Lei H, Yao Z, Li J, Lin J and Cao R 2020 *Chem. Sci.* **11** 87–96
- [36] Zhang R and Warren J J 2020 *J. Am. Chem. Soc.* **142** 13426–34
- [37] Sinha S, Ghosh M and Warren J J 2019 *ACS Catal.* **9** 2685–91
- [38] Kaminsky C J, Wright J and Surendranath Y 2019 *ACS Catal.* **9** 3667–71
- [39] Smith P T, Kim Y, Benke B P, Kim K and Chang C J 2020 *Angew. Chem., Int. Ed. Engl.* **59** 4902–7
- [40] Gao J and Liu B 2020 *ACS Mater. Lett.* **2** 1008–24
- [41] Chang S L Y, Fekete M, Hocking R K, Izgorodina A, Singh A, Zhou F, MacFarlane D R and Spiccia L 2013 *New and Future Developments in Catalysis* (Amsterdam: Elsevier) ch 13 pp 305–39
- [42] Eda G, Yamaguchi H, Voiry D, Fujita T, Chen M and Chhowalla M 2011 *Nano Lett.* **11** 5111–6
- [43] Bertolazzi S, Gobbi M, Zhao Y, Backes C and Samorì P 2018 *Chem. Soc. Rev.* **47** 6845–88
- [44] Stergiou A and Tagmatarchis N 2018 *Chemistry A* **24** 18246–57
- [45] Knirsch K C et al 2015 *ACS Nano* **9** 6018–30
- [46] Er E, Hou H-L, Criado A, Langer J, Möller M, Erk N, Liz-Marzán L M and Prato M 2019 *Chem. Mater.* **31** 5725–34

- [47] Stergiou A, Stangel C, Canton-Vitoria R, Kitauro R and Tagmatarchis N 2021 *Nanoscale* **13** 8948–57
- [48] Jiménez Sandoval S, Yang D, Frindt R F and Irwin J C 1991 *Phys. Rev. B* **44** 3955–62
- [49] Zhang X, Qiao X-F, Shi W, Wu J-B, Jiang D-S and Tan P-H 2015 *Chem. Soc. Rev.* **44** 2757–85
- [50] Yang D, Sandoval S J, Divigalpitiya W M R, Irwin J C and Frindt R F 1991 *Phys. Rev. B* **43** 12053–6
- [51] Wang Y, Wang L, Zhang X, Liang X, Feng Y and Feng W 2021 *Nano Today* **37** 101059
- [52] Wang D, Su B, Jiang Y, Li L, Ng B K, Wu Z and Liu F 2017 *Chem. Eng. J.* **330** 102–8
- [53] Zhang Y, Kuwahara Y, Mori K, Louis C and Yamashita H 2020 *Nanoscale* **12** 11908–15
- [54] Novoselov K S, Jiang D, Schedin F, Booth T J, Khotkevich V V, Morozov S V and Geim A K 2005 *Proc. Natl Acad. Sci.* **102** 10451
- [55] Chang K, Hai X, Pang H, Zhang H, Shi L, Liu G, Liu H, Zhao G, Li M and Ye J 2016 *Adv. Mater.* **28** 10033–41
- [56] Canton-Vitoria R, Scharl T, Stergiou A, Cadranel A, Arenal R, Guldi D M and Tagmatarchis N 2020 *Angew. Chem., Int. Ed. Engl.* **59** 3976–81
- [57] Canton-Vitoria R, Stangel C and Tagmatarchis N 2018 *ACS Appl. Mater. Interfaces* **10** 23476–80
- [58] Wu W, Wei C, Lin X and Xu Q 2018 *Chem. Asian J.* **13** 1293–6
- [59] Peng Q, Wang Z, Sa B, Wu B and Sun Z 2016 *Sci. Rep.* **6** 31994
- [60] Yu X, Rahmanudin A, Jeanbourquin X A, Tsokkou D, Guijarro N, Banerji N and Sivula K 2017 *ACS Energy Lett.* **2** 524–31
- [61] Jariwala D, Howell S L, Chen K-S, Kang J, Sangwan V K, Filippone S A, Turrisi R, Marks T J, Lauhon L J and Hersam M C 2016 *Nano Lett.* **16** 497–503
- [62] Zhang H, Ji J, Gonzalez A A and Choi J H 2017 *J. Mater. Chem. C* **5** 11233–8
- [63] María Girón R, Marco-Martínez J, Bellani S, Insuasty A, Comas Rojas H, Tullii G, Antognazza M R, Filippone S and Martín N 2016 *J. Mater. Chem. A* **4** 14284–90
- [64] Ekspong J, Sandström R, Rajukumar L P, Terrones M, Wågberg T and Gracia-Espino E 2018 *Adv. Funct. Mater.* **28** 1802744
- [65] Gordon R A, Yang D, Crozier E D, Jiang D T and Frindt R F 2002 *Phys. Rev. B* **65** 125407
- [66] Ekspong J, Sharifi T, Shchukarev A, Klechikov A, Wågberg T and Gracia-Espino E 2016 *Adv. Funct. Mater.* **26** 6766–76
- [67] Barraza Alvarez I, Wu Y, Sanchez J, Ge Y, Ramos-Garcés M V, Chu T, Jaramillo T F, Colón J L and Villagrán D 2021 *Sustain. Energy Fuels* **5** 430–7
- [68] Huerta-Flores A M, Bengasi G, Baba K and Boscher N D 2020 *ACS Appl. Energy Mater.* **3** 9848–55
- [69] Meng J, Bi P, Jia J, Sun X and Chen R 2017 *ChemistrySelect* **2** 4882–8
- [70] Wang N, Ma S, Zuo P, Duan J and Hou B 2021 *Adv. Sci.* **8** 2100076
- [71] Ozoemena K I 2016 *RSC Adv.* **6** 89523–50
- [72] Sun K, Xu W, Lin X, Tian S, Lin W-F, Zhou D and Sun X 2021 *Adv. Mater. Interfaces* **8** 2001360
- [73] Wang Y-H, Schneider P E, Goldsmith Z K, Mondal B, Hammes-Schiffer S and Stahl S S 2019 *ACS Cent. Sci.* **5** 1024–34
- [74] Kagkoura A, Arenal R and Tagmatarchis N 2021 *Adv. Funct. Mater.* **31** 2105287
- [75] Murugan C, Ranjithkumar K and Pandikumar A 2021 *J. Colloid Interface Sci.* **602** 437–51
- [76] Bertoluzzi L, Lopez-Varo P, Jiménez Tejada J A and Bisquert J 2016 *J. Mater. Chem. A* **4** 2873–9
- [77] Seah M P 2001 *Surf. Interface Anal.* **31** 721–3